HHS Public Access

Author manuscript

Med Phys. Author manuscript; available in PMC 2020 July 09.

Published in final edited form as:

Med Phys. 2020 June ; 47(6): 2392–2407. doi:10.1002/mp.14124.

Cone-beam CT for imaging of the head/brain: Development and assessment of scanner prototype and reconstruction algorithms

P. Wu, **A. Sisniega**, **J. W. Stayman**, **W. Zbijewski**
Department of Biomedical Engineering, Johns Hopkins University, Baltimore, MD 21205, USA

D. Foos, **X. Wang**
Carestream Health, Rochester, NY 14608, USA

N. Khanna, **N. Aygun**
Department of Radiology, Johns Hopkins University, Baltimore, MD 21205, USA

R. D. Stevens,
Department of Radiology, Johns Hopkins University, Baltimore, MD 21205, USA

Department of Anesthesiology and Critical Care Medicine, Johns Hopkins University, Baltimore, MD 21205, USA

Department of Neurology, Johns Hopkins University, Baltimore, MD 21205, USA

Department of Neurosurgery, Johns Hopkins University, Baltimore, MD 21205, USA

J. H. Siewerdsen[a)]
Department of Biomedical Engineering, Johns Hopkins University, Baltimore, MD 21205, USA

Department of Radiology, Johns Hopkins University, Baltimore, MD 21205, USA

Department of Neurosurgery, Johns Hopkins University, Baltimore, MD 21205, USA

Abstract

Purpose: Our aim was to develop a high-quality, mobile cone-beam computed tomography (CBCT) scanner for point-of-care detection and monitoring of low-contrast, soft-tissue abnormalities in the head/brain, such as acute intracranial hemorrhage (ICH). This work presents an integrated framework of hardware and algorithmic advances for improving soft-tissue contrast resolution and evaluation of its technical performance with human subjects.

Methods: Four configurations of a CBCT scanner prototype were designed and implemented to investigate key aspects of hardware (including system geometry, antiscatter grid, bowtie filter) and technique protocols. An integrated software pipeline (c.f., a serial cascade of algorithms) was developed for artifact correction (image lag, glare, beam hardening and x-ray scatter), motion compensation, and three-dimensional image (3D) reconstruction [penalized weighted least squares (PWLS), with a hardware-specific statistical noise model]. The PWLS method was extended in this work to accommodate multiple, independently moving regions with different resolution (to address both motion compensation and image truncation). Imaging performance was evaluated

[a)]Author to whom correspondence should be addressed. Electronic mail: jeff.siewerdsen@jhu.edu; Telephone: (443) 287-6269.

quantitatively and qualitatively with 41 human subjects in the neurosciences critical care unit (NCCU) at our institution.

Results: The progression of four scanner configurations exhibited systematic improvement in the quality of raw data by variations in system geometry (source-detector distance), antiscatter grid, and bowtie filter. Quantitative assessment of CBCT images in 41 subjects demonstrated: ~70% reduction in image nonuniformity with artifact correction methods (lag, glare, beam hardening, and scatter); ~40% reduction in motion-induced streak artifacts via the multi-motion compensation method; and ~15% improvement in soft-tissue contrast-to-noise ratio (CNR) for PWLS compared to filtered back-projection (FBP) at matched resolution. Each of these components was important to improve contrast resolution for point-of-care cranial imaging.

Conclusions: This work presents the first application of a high-quality, point-of-care CBCT system for imaging of the head/brain in a neurological critical care setting. Hardware configuration iterations and an integrated software pipeline for artifacts correction and PWLS reconstruction mitigated artifacts and noise to achieve image quality that could be valuable for point-of-care detection and monitoring of a variety of intracranial abnormalities, including ICH and hydrocephalus.

Keywords

artifact correction; cone-beam CT; image quality; model-based image reconstruction; point-of-care neuroimaging; traumatic brain injury

1. INTRODUCTION

The imaging performance of cone-beam computed tomography (CBCT) systems with a flat-panel detector (FPD) has advanced markedly in the last 20 yr. However, in many implementations and applications (e.g., dental,[1] ENT,[2,3] and orthopaedic imaging[4,5]), CBCT is still considered suitable only for visualization of high-contrast features, such as bone or surgical instrumentation. Even in CBCT-guided procedures (e.g., image-guided surgery,[6–8] interventional radiology,[9–11] and image-guided radiation therapy[12,13]), the low contrast resolution of CBCT often limits reliable visualization of soft-tissue anatomy. Recent advances in system design, artifacts correction, and three-dimensional (3D) image reconstruction methods open the possibility for improved low-contrast resolution suitable for novel diagnostic imaging tasks. Cone-beam computed tomography systems developed specifically for breast imaging are an example of such capability, offering clear visualization of fibroglandular tissue and masses.[14,15] Cone-beam computed tomography systems for orthopedic imaging have similarly demonstrated visualization of muscle, fat, tendons, ligaments, and cartilage.[4,16] In contrast to conventional multi-detector CT (MDCT), CBCT systems may be implemented in a variety of adaptable, highly portable configurations, making them potentially well suited to point-of-care applications, including bedside imaging in the intensive care unit (ICU) and/or neurological critical unit (NCCU). However, such applications carry a strong requirement for reliable, diagnostic-quality imaging of low-contrast, soft-tissue anatomy (e.g., ~20–80 HU contrast of acute intracranial hemorrhage, ICH). Despite recent hardware and software improvements, this level of imaging

performance poses a major challenge to the current state of the art in CBCTcontrast resolution.

Accurate and reliable detection of ICH is essential to the diagnosis of a number of neurological pathologies, including traumatic brain injury (TBI), hemorrhagic stroke, aneurysm, and postsurgical hemorrhage.[17,18] Noncontrast-enhanced MDCT is commonly the frontline modality for detection, diagnosis, and monitoring of acute ICH, which presents as hyperdense lesions with ~20–80 HU contrast to surrounding parenchyma or cerebrospinal fluid (CSF).[18,19] For ICU or NCCU patients, however, transport to the MDCT scanner is a cumbersome process that requires time, a dedicated transport team, and represents a significant safety and workflow burden.[20–22] For example, Wayhas et al.[21] reported 15%–71% incidence of adverse events when transporting critical care patients to the CT suite, including arterial hypotension and hypertension, increased intracranial pressure, cardiac arrest, change in respiratory rate, and hypoxemia. Despite these risks, transporting a patient to the CT suite is often clinically necessary, resulting in a change of therapeutic management in 25% of imaged patients.[21,22] The high demand for imaging coupled with the burden and safety risk of patient transport underscores the need to develop high-quality, point-of-care imaging for monitoring and management of NCCU patients.

Mobile MDCT systems such as the CereTom (Neurologica, Danvers MA, USA) have the potential to address this need,[22] but early implementations exhibited a variety of sub-optimal image quality characteristics, including nonisotropic spatial resolution and reduced soft-tissue contrast compared to conventional MDCT.[22,23] In this work, we sought to address this need with a portable CBCT system, which carries a number of characteristics that are well suited for point-of-care imaging, including an open gantry, small footprint, portability, relatively low cost, and a single rotation without the need to move the patient for volumetric acquisition. However, while CBCT excels with respect to high spatial resolution, high-contrast tasks as mentioned above, its performance for low-contrast imaging tasks (like ICH detection) is challenged by two major limitations: (a) multiple sources of image artifacts, including x-ray scatter, beam-hardening, lag, glare, truncation, and patient motion; and (b) a high level of image noise and reduced detective quantum efficiency (DQE) compared to MDCT detectors, owing to reduced absorption efficiency and increased electronic noise. In this work, we address these challenges by implementation of scanner hardware design optimization and a comprehensive algorithmic pipeline for artifact correction integrated with iterative model-based image reconstruction (MBIR).

Previous work[24–31] established a number of hardware and algorithmic advances focusing on certain aspects of the limitations mentioned above, leading to the system reported below and evaluated for the first time with human subjects. Hardware aspects include the development of a CBCT scanner prototype platform designed specifically to provide soft-tissue contrast resolution suitable for imaging of brain tissue.[24,25] Algorithmic aspects include artifact correction methods to mitigate the effects of image lag, glare, beam hardening, and x-ray scatter,[26] as well as patient motion compensation[29] and iterative MBIR based on penalized weighted least squares (PWLS) estimation. This PWLS reconstruction method was modified to include a multiresolution approach as a means of reducing the influence of image truncation[32] (e.g., from the head holder) and a statistical noise model that accounts for

quantum noise, electronic noise, and fluence modulation to achieve noise-resolution characteristics beyond that of conventional filtered backprojection reconstruction (FBP).[30,31]

In this work, we: (a) detail four carefully designed iterations in hardware configuration of the scanner prototype; (b) extend the PWLS method to accommodate multiple, independently moving regions with different resolution ("multi-motion, multi-resolution"); (c) propose a fully integrated pipeline of the algorithmic components mentioned above for the CBCT prototype scanner (instead of simply cascading each processing step). The technical performance of the hardware configuration iterations and integrated software pipeline was quantitatively evaluated under realistic conditions in human subjects (NCCU patients with known or suspected intracranial pathologies). Several quantitative measurement metrics were proposed to measure the performance in terms of artifacts and contrast resolution. The potential diagnostic utility in detection, characterization, and assessment of ICH, intraventricular hemorrhage (IVH), hydrocephalus, ventricular shunt, and ischemic lesions is illustrated using example patient images, with clinical diagnostic reader studies forming the subject of future work.

2. MATERIALS AND METHODS

2.A. Point-of-care CBCT head scanner

Previous work detailed the initial design of a prototype CBCT head scanner developed with a combination of task-based imaging performance model optimization[24] and experimentation.[25] In the study detailed below, we implemented four carefully designed variations of the original scanner configuration (denoted C1–C4) to investigate key aspects of hardware and technique protocols. The initial (C1) configuration established the basic setup of the scan procedure. The C2 configuration investigated a longer scan with increased number of projection views, and the C3 configuration added an antiscatter grid. The C4 configuration adapted the system to a more compact geometry, added a bowtie filter for fluence modulation, used a higher tube potential, and allowed faster scan speed. Parameters of the system are summarized in Table I and detailed in sections below. Photographs of the system in C1 and C4 configurations are shown in Fig. 1.

2.A.1. Prototype scanner configurations—The scanner platform included a mobile U-arm gantry with computer-controlled motors for vertical positioning and rotation of the U-arm with a maximum rotation speed of 24°/s and a maximum scan arc of 360°. Four scanner configurations were investigated as detailed below. All configurations included an x-ray tube with a rotating tungsten anode (Mono-bloc, IMD, Grassobbio, Italy) with 150 kJ heat capacity, 17° anode angle, 0.6 FS focal spot size, and tube potential ranging 70–120 kV. Specified inherent filtration for the x-ray tube was 1.4 mm Al equivalent at 75 kV. Additional 0.27 mm Cu filter was included (relatively thick to reduce beam hardening artifacts[27]), and a manual collimator for adjustment of longitudinal FOV (FOVz) was installed.

All configurations featured a flat-panel detector (FPD) (PaxScan 4343CB, Varian, Palo Alto CA) with 43 × 43 cm^2 detection area and 0.139 × 0.139 mm^2 pixel size. The FPD readout gain allowed three options: low gain (LG, 4 pF integrating capacitance), high gain (HG, 0.5

pF integrating capacitance), and dual gain (DG, combining 0.5 pF HG and 4 pF LG in alternate detector rows). Hardware binning was set to 3 × 3 (0.417 × 0.417 mm^2 pixel size) in single gain (HG/LG) mode, and to 4 × 2 (0.556 × 0.278 mm^2 pixel size) in DG mode.

2.A.2. The C1 configuration—The C1 configuration was based on previously reported task-based imaging performance optimization[24] and provided the basic platform for development of subsequent modifications C2–C4. The system geometry had source-to-axis distance (SAD) = 550 mm and source-to-detector distance (SDD) = 1000 mm. The system was set to acquire 450 projections over a 360° scan arc. The FPD was read in dual gain (DG) mode, which improved dynamic range compared to HG mode, without increasing the electronic noise level in highly attenuating regions of the head. Readout speed for this mode was 15 proj/s, resulting in a total acquisition time of 30 s for the 450 projections. A photograph of the scanner in this configuration is shown in Fig. 1(a).

2.A.3. The C2 Configuration—In this configuration, the number of projections was increased to 900 (without change in mAs/ pulse) to investigate the benefits of reduced quantum noise. The scan time increased proportionately to 60 s. To maintain the same dose–length product (DLP, and therefore effective) as in C1, the FOVz was reduced accordingly, from 24 to 12 cm. All other system parameters were identical to those in the C1 configuration.

2.A.4. The C3 configuration—For the C3 configuration, an antiscatter grid was installed to assess the benefits of increased scatter rejection. We used an 8:1 one-dimensional linear focused grid with lead lamellae, aluminum interspacers, and focal distance compatible with the scanner SDD. The grid was placed in a “horizontal” orientation — that is, gridlines perpendicular to the axis of rotation of the U-arm. Compared to a “vertical” arrangement, this orientation is more robust to gridline artifacts and offers slightly better scatter rejection in head imaging.[33,34] A small number of scans (N = 3) in the C3 configuration were acquired at 120 kV to establish whether the more homogeneous photon fluence, reduced beam hardening, and increased transmission to the detector were advantageous for image quality.

2.A.5. The C4 Configuration—The C4 configuration [shown in Fig. 1(b)] provided the majority of human subjects’ data. It included several modifications to the system hardware and acquisition protocol. First, the possibility of a more compact geometry setting was tested, by reducing SDD from 1000 to 832 mm. An initial configuration with SDD = 732 mm was also investigated (N = 3) and soon judged to be too compact to operate in a manner that was comfortably free from collision in an open gantry. Second, a higher tube potential (120 kV, also tested for a small subset of subjects in C3) was adopted. Thirdly, an Al bowtie filter was incorporated to improve dose distribution, further reducing x-ray scatter (in combination with the antiscatter grid) and increasing dynamic range.[27] The bowtie filter was designed to give a spatially uniform fluence behind a water cylinder of 120 mm (determined in Ref. [27]) diameter at SAD = 550 mm. A cylindrically symmetric (“1D”) bowtie filter was found to be sufficient — without saturation in the superior aspect of the skull — due to self-attenuation in the crown of the skull.[27]

Patient motion, ranging from a few mm to a few cm, was evident early in the study, despite the use of light motion restraints (head holder and a Velcro strap over the forehead) and coaching subjects to remain still. To address this issue, the C4 system implemented several strategies to reduce the scan time to 17 s, compared to 60 s in C2–C3: (a) the scan arc was reduced from 360° to 220°; (b) the angular sampling density was reduced from 2.5 to 1.8 proj/°; and (c) the detector readout mode was changed to HG, increasing the frame rate to 24 proj/s from 15 proj/s for DG, made possible because the bowtie filter compressed the dynamic range of the data, obviating the need for DG readout. As a result of strategy (a) and (b), the number of projections was reduced to 400 in this configuration, compared to 900 in C2–C3; since the mAs per projection was unchanged, the FOVz was increased back to 24 cm (as in C1) with no increase in DLP or effective dose.

2.B. Artifact correction and image reconstruction algorithms

Cone-beam computed tomography images were reconstructed following the workflow in Fig. 2, consisting of the following major components: (a) artifact correction methods for lag, glare, beam hardening (BH) and scatter;[26] (b) a motion estimation algorithm incorporating multiple independently moving ROIs within the FOV;[29] (c) image reconstruction using a MBIR (PWLS) method, which was extended in this work to accommodate multiple, independently moving regions with different resolution ("multi-motion, multi-resolution[32]"). The proposed MBIR method also implemented modified statistical weights to account for electronic and quantum noise (including fluence modulation from bowtie filter).[30] These components and their integration methods are detailed below:

2.B.1. Artifact correction: lag, glare, beam hardening, and scatter—

The raw projections were first preprocessed with detector defects and offset corrections, and gain normalization. In C1–C3 configurations, the preprocessing also included merging the data read in the DG readout modes.[27] This was not required in the C4 configuration, which was operated only in the HG readout mode. However, because the C4 configuration included a bowtie filter, the gain normalization included an additional polyenergetic correction step to account for the spatially varying x-ray spectrum.[27,31]

The preprocessed projections were then corrected for detector lag through temporal deconvolution using a measured lag response function,[35] followed by veiling glare correction through spatial deconvolution using the long-range tails of the detector point-spread function (PSF).[36] Note that this response function accounted not only for detector veiling glare, but also includes other low-frequency components of the PSF, such as off-focal radiation.

Scatter and BH were corrected iteratively. In each iteration, the Joseph-Spital (JS)[37] approach incorporating water and bone-induced BH was used to generate a BH-corrected FBP reconstruction. This reconstruction was then segmented to generate a variable density, air-water-bone object model for a fast Monte Carlo (MC) scatter simulator. The MC implementation achieved scatter estimation with a runtime of ~15 s/projection, owing to acceleration by variance reduction, GPU acceleration, and "sparse" tracking (low number of photons and projection angles) followed by kernel denoising.[26] The MC scatter estimate was

subtracted from the preprocessed projections to provide input to the next iteration of BH and scatter correction. Three iterations were performed for the results shown below. The projections generated after three passes of the JS correction and scatter estimation/subtraction were used as input for motion estimation (detailed in Section 2.B.2). After the motion estimation, another pass of JS correction (but not scatter estimation) was performed, as explained below. A modification to the scatter estimation method used in this work was to optionally use a PWLS reconstruction in the final iteration of MC estimation (especially for datasets with large truncation). Doing so improved scatter estimation of the truncated region via the penalty term in PWLS, as indicated by the dashed line feedback loop in Fig. 2.

Due to polyenergetic correction applied as a preprocessing step, JS correction does not need to be modified to account for the introduction of bowtie filter in C4 configuration. However, MC scatter estimation required modification by implementing a weight factor applied to each tracked photon to account for the angle- and energy-dependent attenuation in the bowtie.[37] Similarly, we implemented another weight factor based on grid transmission computed from the analytical model of Day and Dance[38] to account for the introduction of the antiscatter grid in C3 and C4.

2.B.2. Multi-motion estimation—A motion estimation algorithm was implemented based on an image-based autofocus approach to estimate the rigid displacements of the head in each projection view by maximizing an image sharpness criterion. Similar algorithms have been previously applied to CBCT extremities imaging,[39] although previous implementations typically assumed a single motion pattern for the entire reconstructed volume. In this work, we extended the autofocus algorithm to accommodate multiple independently moving ROIs.[29] In particular, two ROIs were defined as depicted in Fig. 3: (a) ROI for the head where we anticipated the most substantial motion (denoted “moving” and associated with motion trajectory T_M); and (b) ROI for the remainder of the FOV (typically the head support), which remained mostly stationary (denoted by motion trajectory T_S). The autofocus cost-function was computed as the sum of the sharpness metrics of the two ROIs. Motion trajectories in these two ROIs were jointly estimated by maximizing the autofocus objective using a derivative-free covariance matrix adaptation evolution strategy (CMA-ES) optimizer.[40]

Among the artifact corrections described in Section 2.B.1, the BH and scatter corrections depend on patient motion through their dependency on system geometry. Initial empirical studies indicated that patient motion had negligible impact on the low-frequency scatter distributions and thus, to reduce computational load, we did not incorporate the estimated motion profiles in MC scatter estimation. However, the BH correction step needed to be reapplied after motion estimation (as indicated by the double-arrows in Fig. 2) to avoid streak artifacts. Empirical studies also indicated that another round of motion estimation after reapplying BH correction was not necessary (i.e., motion estimation and BH correction were not performed iteratively for the sake of computation efficiency). After reapplying the BH correction step, the corrected projections and the estimated motion trajectories for each ROI were used as the input to the final PWLS reconstruction step as detailed in Section 2.B.3.

2.B.3. Model based image reconstruction—The conventional PWLS method performs image reconstruction by minimizing an objective function typically formulated as:

$$\hat{\mu} = \arg\min_{\mu} = \frac{1}{2}\|\mathbf{A}\mu - l\|_{\mathbf{W}}^2 + \beta\mathbf{R}(\mu) \quad (1)$$

where μ is a vector representing the reconstructed image, $\mathbf{A}$ denotes the linear forward projection operator, l is the x-ray attenuation measurement in the line integral domain, and $\mathbf{W}$ is a diagonal matrix containing a statistical weight for each measurement, which is conventionally assumed to be an estimate of the inverse of the variance of that measurement, $\boldsymbol{R}(\mu)$ is an image roughness penalty term (Huber loss function,[41] which penalizes pairwise differences between voxels in a first-order neighborhood around each voxel), and β is a scalar controlling the relative strength of the penalty.

Multi-motion and multiresolution in PWLS: The imaging FOV of this system is often not large enough to completely accommodate the head holder, other positioning devices, and additional hardware (e.g., ventilation tubes), resulting in data truncation. In MBIR methods such as PWLS, the complete support of the acquired projections needs to be included in the reconstruction field-of-view (RFOV). However, extension of the RFOV to the required size results in very large reconstruction volumes, leading to a prohibitive computational burden. To address this issue, we adapted a multiresolution reconstruction approach[32] in which the total volume was split into two regions: a main (inner) region covering the head with finer voxel size; and an extended (outer) region with coarser voxel size to mitigate truncation artifacts from the head holder while introducing minimal increase in computational complexity.

We extended the multiresolution PWLS method to accommodate multiple, independent regions of motion (Section 2.B.2) by further dividing the inner region into a moving and a static region, which are referred to as μ_{FM} (fine, moving), and μ_{FS} (fine, static), respectively (shown in Fig. 3). Since the head was not within the outer region, the outer region was reconstructed using a static motion trajectory (μ_{CS}, coarse, static).[42]

Following the derivation in Ref. [32], forward projection ($\mathbf{A}\mu$) was decomposed:

$$\mathbf{A}\mu = \begin{bmatrix}\mathbf{A}_{FM} & \mathbf{A}_{FS} & \mathbf{A}_{CS}\end{bmatrix}\begin{bmatrix}\mu_{FM} \\ \mu_{FS} \\ \mu_{CS}\end{bmatrix} \quad (2)$$

where μ_{FM}, μ_{FS}, and μ_{CS} are the reconstructed volumes in the three regions defined above, $\mathbf{A}_{FM}$, $\mathbf{A}_{FS}$ and $\mathbf{A}_{CS}$ are the corresponding forward projection operators, which incorporated precomputed motion trajectories described in Section 2.B.2, with different voxel grid definitions. The transition between regions with different motion trajectories (μ_{FM} and μ_{FS}) was set discontinuous, which was not anticipated to have notable effect, since the intermediate region is mostly air (or a pillow placed between the head and the head holder). The transition between regions of different resolution (μ_{FM} and μ_{FS}, to μ_C) was assumed discontinuous as well, which was again a reasonable choice since the transition region did

not contain clinically relevant anatomical structures. Regularization strength [β in Eq. (1)] was set to the same value for μ_{FM} and μ_{FS}, and was empirically set to be 100 × higher in μ_C (since only used for truncation handling).

Modified statistical weights in PWLS: Under the assumption of Poisson distributed quantum noise, the variance in the measurement is typically approximated by the measurement itself. However, to incorporate contributions from electronic noise and fluence modulation, the statistical weights [**W** in Eq. (1)] were modified (and denoted **W***) to the following form[30]:

$$\mathbf{W}_{\mathbf{i}}^{*} \approx \frac{\frac{\Delta_i^2 \cdot m_i^2}{I_0}}{\frac{\Delta_i \cdot m_i}{I_0} + \frac{\sigma_{e,i}^2}{\gamma I_0}} \tag{3}$$

where m_i is the measurement, i is the measurement index, I_0 is the mean flood-field data, γ is a gain term that reflects factors of system gain, system blur, and detector lag on the quantum noise,[30] $\sigma_{e,i}^2$ is the electronic noise (spatially varying for dual-gain readout modes), and Δ_i is the fluence modulation map, which was computed as the ratio between flood-field data with and without the fluence modulator (bowtie filter).[30,31]

With these modifications, the PWLS objective function was minimized using the separable quadratic surrogates (SQS) method with ordered subsets (OS-SQS),[43] with 80 iterations and 10 subsets. Optimization updates became negligible after 80 iterations (L2-norm of the update below 0.05% of the L2-norm of the reconstructed image). Forward and backprojection operations were performed with matched separable footprint forward and backward projectors,[44] and a Huber penalty of pairwise voxel differences over six first-order neighborhood voxels was used for the regularization term.[45]

All images (fine resolution region) were reconstructed with a 0.44 × 0.44 × 0.44 mm^3 voxel size (26.4 ×26.4 × 22 cm^3 RFOV). The multiresolution approach extends the RFOV to 35.2 × 35.2 × 30 cm^3 (1.76 × 1.76 × 1.76 mm^3 voxel size in the extended region). The display setting for slice visualization (axial, sagittal, or coronal planes) was set to 3 mm slice thickness by slice averaging, which is the usual setting for diagnostic evaluation in MDCT of the brain.

2.B.4. FBP reconstruction—Filtered backprojection reconstruction based on the Feldkamp-Davis-Kress (FDK) algorithm was also performed as a comparison to PWLS reconstruction. Both FBP and PWLS used artifact corrections as detailed in Section 2.B.1. A two-dimensional (2D) Hann filter in both u and v direction was implemented to get a fairer comparison with PWLS method which used between-plane regularization. The forward projection operator in FBP was modified to use the pre-estimated head motion trajectory (region μ_{FM}, detailed in Section 2.B.2) for the entire RFOV, which was extended to 35.2 × 35.2 × 30 cm^3 (0.44 mm isotropic voxel size) to reduce truncation artifacts (same size as the extended RFOV in PWLS). As with the PWLS method, the displayed slice thickness for axial, sagittal, or coronal planes was set to 3 mm by slice averaging.

2.C. Evaluation in human subjects

A study was conducted under Institutional Review Board (IRB) approval to evaluate the performance of the proposed hardware configuration iterations and integrated software pipeline in human subjects. The study cohort included patients in the NCCU with known or suspected ICH and/or hydrocephalus. The protocol involved acquisition of a single CBCT scan immediately following the patient's routine MDCT scan [shown in Fig. 1(a)].

A total of 54 subjects were imaged, with 13 excluded for the following reasons: 10 were agitated and not responsive to verbal instructions, resulting in severe motion and highly inconsistent projection data that was not suitable for motion compensation; and three subjects had extensive external hardware (ventilators etc.) that prevented proper positioning of the head inside the gantry. Nine out of the ten motion-related exclusions were with C2 or C3 configurations, demonstrating the benefits of reduced scan time in C1 and C4. After exclusions, 41 subjects were used in the study as shown in Table I: five subjects were imaged on C1, six on C2, nine on C3, and 21 on C4.

2.D. Quantitative performance evaluation in human subject images

Challenges to objective, quantitative metrology in human subject data are numerous, particularly for a complex range of imaging conditions (C1–C4 configurations), artifacts, and underlying anatomy/pathology. Without ground truth, quantitation of image artifacts (e.g., shading and streaks) lacks standard metrology and can be strongly dependent on ROI placement. Moreover, the metrics should be pertinent/ translatable between all evaluated subjects even under disparate scan or reconstruction conditions. Moreover, imaging performance metrology for nonlinear reconstruction methods (such as PWLS) should recognize assumptions and limitations in quantifying noise-resolution tradeoffs (e.g., nonlinearity and nonstationarity).

In this work, we assessed the technical performance of the scanner and algorithms in terms of objective, quantitative metrics computed from images of the 41 human subjects, including contrast (with respect to soft-tissue structures), contrast-to-noise ratio (CNR), spatial resolution (with respect to soft-tissue edges), image uniformity, and magnitude of streak artifacts. Since the noise properties of both FBP and PWLS can be controlled via parameter settings (cutoff frequency in FBP, and β in PWLS, which can reduce noise at the expense of spatial resolution), the spatial resolution was matched subject-by-subject to provide a fair comparison of noise performance. The improvements gained by each of the C1–C4 scanner configurations are also quantified. The results are complemented by qualitative evaluation of representative images from the study. A reader study in which expert observers evaluate images with respect to particular imaging tasks is the subject of ongoing work.

The following subsections summarize the methods and proposed metrics for objective assessment of basic imaging performance from the study.

2.D.1. Non-uniformity (NU)—Image nonuniformity (NU) quantified biases and artifacts related to low-frequency fluctuations in the reconstructed image. Twelve ROIs of size 16 × 16 × 8 voxels were used for NU evaluation in each subject. The ROIs were placed in

relatively homogeneous regions of brain parenchyma throughout the interior of the skull as illustrated in Fig. 4(a). Regions of pathology (as evident in MDCT) — for example, edema or ischemia — were avoided. The NU was computed as the standard deviation of the mean attenuation values from each ROI:

$$\mathrm{NU} = \sigma(\overline{\mu_{ROI}}) . \tag{4}$$

2.D.2. Motion artifacts ($\sigma_{\mathrm{streaks}}$)—Effects of motion usually manifest as high-frequency streak artifacts that are more prominent on high-contrast features. Streak artifacts were characterized by:

$$\sigma^2_{\mathrm{streaks}} = \overline{\sigma^2_{\mathrm{total}}} - \sigma^2_{\mathrm{quantum}} \tag{5}$$

where σ_{total} was the STD measured within four streak contaminated ROIs (16 × 16 × 8 voxels), and $\sigma_{\mathrm{quantum}}$ was measured on a nearby ROI (16 × 16 × 8 voxels), free of streak artifacts. Since the variance within an ROI involves contributions from both motion-related streak artifacts and quantum noise, a squared subtraction with the quantum variance removes effects of the latter.

Like the computation of NU, ROIs were placed on a persubject basis in regions with visible streak artifacts in otherwise homogeneous anatomy. Example ROI placement for σ_{total} and $\sigma_{\mathrm{quantum}}$ is shown in Fig. 4(c). While motion estimation/ compensation was consistently performed for all 41 subjects, $\sigma_{\mathrm{streaks}}$ was only analyzed for 25 subjects that exhibited visible streak artifacts prior to motion compensation.

2.D.3. Spatial resolution—Spatial resolution was evaluated in soft-tissue structures using the boundary between the lateral ventricle and the surrounding brain parenchyma [see Figs. 4(b) and 4(d)]. The boundary position was estimated using a Canny edge detection method[46] and a set of 60 edge profiles were measured following lines perpendicular to the edge. The spatial resolution was then estimated as the width of the edge spread function (ESF) obtained by numerical fit of an error function to the edge profile measurements:

$$f(x) = a - \frac{c}{2}\mathrm{erf}\left(\frac{x-r}{\sqrt{2}\sigma_{\mathrm{ESF}}}\right) \tag{6}$$

where erf is the error function, σ_{ESF} denotes the ESF width, r represents the distance to the edge in mm, c is the contrast between the ventricle and the brain parenchyma, and a approximates the attenuation value of the brain parenchyma. The spatial resolution was matched between FBP and PWLS reconstructions by tuning the cutoff frequency for FBP (cutoff frequency ~5%–100% of the Nyquist frequency) and the penalty strength for PWLS ($\beta \sim$ 1e2–1e6). While the ESF width is not completely representative of the spatial resolution of the entire volume, it provides a reasonable starting point for fair comparison of noise characteristics between FBP and PWLS, as described in the following section.

2.D.4. Soft tissue contrast-to-noise ratio—Soft tissue contrast was defined as the difference in attenuation value between two ROIs, one placed at the brain parenchyma and a

second one placed at the (lateral) ventricle [see Fig. 4(b)]. The soft tissue contrast-to-noise ratio (CNR) was calculated as:

$$\mathrm{CNR} = \frac{\left|\overline{\mathrm{ROI}}_{\mathrm{parenchyma}} - \overline{\mathrm{ROI}}_{\mathrm{ventricle}}\right|}{\sigma_{\mathrm{ventricle}}} \quad (7)$$

where $\sigma_{\mathrm{ventricle}}$ is the standard deviation within the ventricle ROI. Since the spatial resolution and noise properties are spatially varying in PWLS reconstructions,[47] the measurement ROIs (for the parenchyma and ventricle) were placed in the same general area of the volume and as close as possible to the ROIs for spatial resolution assessment. This allowed comparison between CNR measurements obtained with PWLS and FBP, at matched spatial resolution.

3. RESULTS

3.A. Artifacts correction

Figure 5 shows the effects of the artifacts correction pipeline (including lag, glare, beam hardening, and scatter) in two subjects imaged with the C1 and C4 configurations, respectively. All other aspects of the artifacts correction pipeline were kept fixed to isolate the effects of artifacts correction and system configuration in this figure. All images in this section were reconstructed with FBP.

The first row of Figs. 5(a)–5(c) shows a representative dataset acquired in a subject with a left ventricular catheter using the C1 configuration at different stages of the artifacts correction pipeline. Comparison of Figs. 5(a) and 5(b) (scatter corrected) demonstrates major reduction of shading artifacts (especially in the central region) and nonuniformity (overall NU reduced from 61.2 to 32.5 HU; ROIs placed in relatively uniform region with reference to MDCT). However, strong nonuniformity is still evident, including residual shading artifacts in the central region of the brain and blooming artifacts around the skull. Comparison of Figs. 5(b) and 5(c) shows further improvement by applying the remaining steps of the artifacts correction pipeline: lag, glare, and beam hardening correction. The overall NU was further reduced from 32.5 to 13.5 HU.

The second row of Fig. 5 depicts a representative dataset acquired in a subject with a hypodense lesion in bilateral frontal lobes and in the right temporal lobe, using the C4 configuration at different stages of the artifacts correction pipeline. As mentioned in Section 2.D.1, the hypodense lesion region (as evident in MDCT) was avoided in ROI placement (column (c)). Comparison of the images in column (a) and (d) for the C1 (first row) and C4 (second row) configurations showed noticeably improved quality of the raw image data in C4. For example, anatomical structures such as the lateral ventricles are visible in C4 even prior to application of the artifacts correction pipeline, and NU for the uncorrected images was reduced from 61.2 for C1 to 39.5 HU for the C4 configuration. This is primarily due to the use of the antiscatter grid and bowtie filter. In addition to the reduction in the magnitude of artifacts, their nature and distribution are different as well. For example: (a) scatter artifacts presented as cupping artifacts centered around the center of the brain in C1, but they showed as capping artifacts centered around the bowtie center in C4, since scatter was

modulated by the shape of the bowtie filter; and (b) blooming artifacts around the skull were largely reduced in C4 compared to C1, most likely due to the prehardening effect caused by the bowtie filter in C4 configuration.

Quantitative analysis of the trends underlying the images in Fig. 5 are summarized in Fig. 6 for the 41 subjects evaluated in the study. With the full artifacts correction pipeline, NU was reduced from a median value of ~38 HU for the uncorrected image to ~10 HU for the fully corrected image, with a fractional improvement of ~70% [as shown in Fig. 6(b)]. X-ray scatter correction accounted for ~60% of the total NU reduction, as shown in Figs. 6(a)–6(b).

Figure 6(c) shows the distribution in root-mean-square-difference (RMSD) across all subjects between the uncorrected images and the fully corrected images as a function of the scanner configuration (C1–C4). The distribution in RMSD between scatter-corrected images and the fully corrected images is shown in (d). Since the FOVz was varied from C1 to C4, RMSD was only calculated for the central 50 slices (2 cm FOVz). The decreasing RMSD from the original C1 configuration to the final C4 configuration illustrates the progressive improvement in the quality of raw data. The enhancement in the raw data quality for the C2 configuration can be mostly attributed to the smaller FOVz, which mostly acted on scatter artifacts. The C3 configuration further improved raw data quality via the antiscatter grid, which mostly acted on scatter artifacts as well. Therefore the RMSD for C2 and C3 are lower than C1 in Fig. 6(c) and are comparable to C1 in Fig. 6(d). In addition to increased scatter rejection, the C4 configuration resulted in lower beam hardening artifacts from the prehardening effect provided by the bowtie filter coupled with a higher tube potential (120 kV in C4 compared to 100 kV in C1–C3). This results in RMSD reduction both in (c) and (d).

3.B. Multi-motion compensation

Figures 7(a)–7(c) show an example subject with moderate (a few mm) head motion during the CBCT scan. All other aspects of the artifacts correction/reconstruction pipeline were kept fixed to isolate the effects of motion compensation. Compared to the image without motion compensation, the single motion compensation reconstruction (using single motion trajectory for the entire FOV) showed noticeable improvement in motion artifacts, with better visualization of the ventricular shunt and a reduction in streak artifacts (σ_{streaks} reduced from 23.4 to 14.6 HU after single motion compensation). (Note that all images in this section were reconstructed with PWLS.) However, the single motion reconstruction exhibited residual streak artifacts from the head holder — that is, the head moved *within* the head holder (different motion trajectories for head and head holder). Comparison of Figs 7(b) and 7(c) shows further improvement when using the multi-motion compensation reconstruction — for example, streak artifacts associated with the head holder [pink arrow in Fig. 7(b)] was reduced with multi-motion compensation, and overall magnitude of streak artifacts was further reduced to $\sigma_{\text{streaks}} = 13.2$ HU.

Imaging performance without and with multi-motion compensation is further quantified in Figs. 8(a)–8(b). Motion-related streak artifacts were reduced by ~40% with multi-motion compensation. Motion compensation also showed benefit beyond reduction of streak

artifacts. For example, the method improved visualization of soft-tissue boundaries as illustrated in Fig. 8(c), where sulci and soft-tissue edges throughout the brain are more distinct after motion compensation.

3.C. Model-based image reconstruction (PWLS)

Figure 9 shows example images reconstructed with FBP and the proposed PWLS method, with other aspects of the pipeline (artifacts correction, motion compensation, etc.) held fixed. Spatial resolution for FBP and PWLS reconstructions was matched to give equivalent σ_{ESF} for soft-tissue boundaries near the center of the image (lateral ventricles and brain parenchyma). Visual comparison suggests subtle improvement in noise characteristics for PWLS, showing a slight reduction in noise magnitude [e.g., $\sigma_{ventricle}$ reduced from 6.1 to 4.7 HU in Fig. 9(a)] and a more uniform noise texture (i.e., reduced directional noise correlation). The qualitative difference is fairly subtle, and green arrows mark example low-contrast structures for which delineation is qualitatively improved in PWLS compared to FBP [see, for example., the posterior aspect of the lateral ventricle in Fig. 9(a) and the sagittal sulcus in Fig. 9(b)].

Figure 10 quantifies the noise-resolution tradeoffs for FBP and PWLS, demonstrating a ~15%–20% improvement in CNR for PWLS over a wide range of spatial resolution. Comparison of the CNR (measured between CSF in the lateral ventricle and the surrounding brain parenchyma) between FBP and PWLS across all subjects in the study is shown in Fig. 10(b), each with matched spatial resolution. The ratio (Q_{CNR}) shows a median improvement in CNR of ~15%, with a lower bound of ~1% (i.e., PWLS never underperformed compared to FBP in the current study), and the improvements in some subjects were as large as ~32%.

4. DISCUSSION AND CONCLUSIONS

This work presented a series of high-level engineering design iterations in scanner hardware, a PWLS method extended to multi-motion/ multiresolution reconstruction, and a fully integrated artifacts correction and reconstruction pipeline for CBCT in point-of-care imaging in the NCCU. The technical performance of the hardware/ software developments was evaluated quantitatively in images of 41 human subjects. Such a system could significantly ameliorate workflow and safety considerations related to patient transport from the NCCU to the CT suite.

A number of artifacts correction and reconstruction algorithms were integrated in this work, including correction of lag, glare, beam hardening, scatter, motion, and truncation artifacts, and model-based reconstruction (PWLS) with a statistical noise model considering quantum noise, electronic noise, and fluence modulation. Instead of simply cascading those algorithms, the integrated pipeline incorporates the interaction between them, for example, (a) interaction of BH/scatter correction with motion estimation (detailed in Section 2.B.2); and (b) modification of the forward projection operator in PWLS to account for multiple independently moving regions with different resolution (detailed in Section Multi-motion and multiresolution in PWLS).

The quantitative imaging performance characteristics measured across 41 subjects demonstrated steady improvement from each component of the integrated artifacts correction and reconstruction pipeline. Image NU was reduced by ~70% with artifact correction methods (lag, glare, beam hardening, and scatter). Multi-motion compensation reduced motion-induced streak artifacts (σ_{streaks}) overall by ~40%. The PWLS algorithm yielded a ~15% improvement in CNR compared to FBP at matched resolution, with improvement up to ~30% in some subjects. The gains in imaging performance were visually evident as well [e.g., comparing the conventional "raw" FBP reconstructed CBCT images as in Fig. 5(a) with images after applying artifacts correction and PWLS reconstruction as in Fig. 7(c), second column of Fig. 8(c), and second columns in Fig. 9].

Quantitative metrics measured across 41 subjects also demonstrated steady improvement in the quality of raw data across the four configurations of the scanner, showing overall reduction in RMSD (between the raw and the fully corrected image) of ~65%. The C2 configuration resulted in ~28% improvement in RMSD over C1, due primarily to reduced scatter for the smaller FOVz. The C3 configuration improved RMSD by ~30% compared to C2 by virtue of an antiscatter grid. The C4 configuration improved RMSD by ~45% compared to C3 by incorporation of a bowtie filter and higher tube potential. Finally, the C4 configuration decreased the image acquisition time from 60 s (in C2 and C3) to ~17 s, thereby reducing the likelihood and severity of patient motion effects. For example, 9/10 of the subjects exhibiting severe motion artifact (thus excluded from evaluation) were from C2 and C3 configurations.

Overall, the resulting images demonstrate clear visualization of ICH and IVH, reliable assessment of ventricular shunt placement, and the potential to assess or monitor known ischemic lesions (which are challenging even in MDCT). Bone visualization — not included in the results shown above for reasons of brevity — was excellent, and FBP with a high-resolution filter is likely sufficient for assessment of cranial features — for example, differentiation of fracture from suture lines.

The results are promising with respect to this challenging application of CBCT and suggest a number of points warranting future investigation. First is the assessment of image quality with respect to specific clinical tasks — for example, expert assessment of the sufficiency of image quality for monitoring known lesions or detecting emergent abnormalities. While the study involved both CBCT and MDCT images, a meaningful head-to-head comparison of diagnostic performance requires careful consideration of numerous technical and logistical factors. In the current study, there is no reason to think that CBCT would match or exceed the performance of MDCT; it almost certainly will not, and direct comparison of CBCT and MDCT images was not included in the current study. (Note also that the dose for CBCT scans in this study was ~40%–46% less than the dose for MDCT.) Given the quantifiable improvements in CBCT image quality achieved by the methods reported in this work, the pertinent question to a future expert reader study is whether portable CBCT acquired at the point of care is sufficient in monitoring known pathologies (thereby saving patient transport to the CT scanner) and/or reliably detecting emergent pathologies as they arise.

Images of the human subjects used in this work provide evidence in support of the feasibility of mobile CBCT for evaluation of acute brain lesions, as illustrated in Fig. 11. Figure 11(a) shows axial and sagittal images of a subject with a small subdural hematoma. Two foci of hemorrhage are visible overlying the right frontal lobe, and despite their small size, low contrast, and proximity to the skull (a region challenged by beam-hardening effects), initial assessment suggests that delineation of the boundary and measurement of the size of each can be reliably performed. Figure 11(b) shows images of a subject with hydrocephalus treated with a ventricular shunt. The location of the shunt with respect to the ventricle is clear in both axial and sagittal views — in this case, the tip of the shunt free-floating in the atrium of the right lateral ventricle. Figure 11(c) shows images of a subject with pituitary tumor with hemorrhagic transformation, and while the visibility of the tumor is challenged by residual artifacts from the skull base (also a common problem in MDCT of pituitary tumors), the presence and size of the tumor can still be reasonably assessed. Figure 11(d) shows axial images of a subject with bilateral ischemic lesions (hypo-dense regions) that are distinguishable from shading artifacts. Such lesions are challenging to discriminate from residual shading artifacts even in MDCT, but the images may be sufficient for monitoring the status of such lesions previously identified in MDCT or MRI. Figure 11(e) shows axial images from a subject with intraventricular hemorrhage (IVH). Large hemorrhages are clearly visible from the image, and their sizes and boundaries can be evaluated with confidence.

Another important point is the extent to which the proposed artifact correction and reconstruction algorithms can be implemented with clinically acceptable runtime — an important consideration for incorporation in realistic clinical workflow. The total runtime for image processing and reconstruction in this work was ~8 h, which breaks down to: ~1.5 h for artifacts correction; ~1.5 h for motion estimation; and ~5 h for PWLS reconstruction. Relatively little effort was paid to code optimization or runtime acceleration in the current work, which focused mainly on feasibility and evaluation of image quality. A number of strategies for reducing the runtime include: (a) implementation on multi-GPU architectures for MC scatter estimation, motion estimation, and MBIR; (b) replacing the time-consuming MC scatter estimation with kernel based or machine learning based scatter estimation method;[48,49] (c) use of 3D-2D registration or machine learning approaches to precondition the estimation of the motion trajectory;[29] (d) replacing the time-consuming separable footprint forward and back projector with simpler, more efficient, yet less accurate projector models (e.g., Siddon forward projector[50] and Peter's backprojector[51]); and (e) using momentum-based acceleration approaches previously applied to MBIR, like the Nesterov method.[52] Such methods are the subjects of ongoing work, as described in Ref [53,54] for example, where runtimes <30 s were reported for datasets of comparable size.

Additional and potentially more advanced artifact correction and image reconstruction techniques can also be envisioned. These include metal artifact reduction (MAR) methods, such as KC-MAR or KC-Recon to account for the presence of metal instrumentation.[55,56] More advanced regularization schemes could be incorporated, including selection of regularization weights in a manner to optimize local task-based signal-to-noise characteristics.[57] The system model intrinsic to the MBIR method could be advanced to include effects of detector blur and correlated noise.[58] Among the most important areas for

future improvement, however, is compensation/ correction of patient motion effects. Even for the relatively stable anatomy associated with the head, motion compensation was an important part of the image processing chain described above and was challenged by nonrigid components (neck and jaw) and motion of the patient separate from that of the head holder, motivating more advanced multi-motion compensation method.[59] Hardware modifications that resulted in faster scan speed was shown to reduce susceptibility to motion artifacts, but motion management is likely to persist as an important aspect of achieving diagnostic quality in CBCT. Additional future hardware modifications may include incorporation of 2D antiscatter grid.

ACKNOWLEDGMENTS

This work was supported by NIH R01-EB-017226, NIH U01-NS-107133, and academic-industry partnership with Carestream Health (Rochester NY). Dr. Jennifer Xu and Dr. Hao Dang (Biomedical Engineering, Johns Hopkins University) contributed previous work on the development of the scanner prototype and reconstruction algorithms. Dr. Jason Hostetter (Radiology, Johns Hopkins University) provided additional feedback on image quality. The clinical study was coordinated by Eusebia Calvillo (Anesthesia and Critical Care, Johns Hopkins Medical Institution).

REFERENCES

1. Baba R, Ueda K, Okabe M. Using a flat-panel detector in high resolution cone beam CT for dental imaging. Dentomaxillofacial Radiol. 2004;33:285–290.
2. Miracle AC, Mukherji SK. Conebeam CT of the head and neck, part 2: clinical applications. Am J Neuroradiol. 2009;30:1285–1292. [PubMed: 19461061]
3. Hodez C, Griffaton-Taillandier C, Bensimon I. Cone-beam imaging: applications in ENT. Eur Ann Otorhinolaryngol Head Neck Dis. 2011;128:65–78. [PubMed: 21459066]
4. Zbijewski W, De Jean P, Prakash P, et al. A dedicated cone-beam CT system for musculoskeletal extremities imaging: design, optimization, and initial performance characterization. Med Phys. 2011;38:4700–4713. [PubMed: 21928644]
5. Koskinen SK, Haapamäki VV, Salo J, et al. CT arthrography of the wrist using a novel, mobile, dedicated extremity cone-beam CT (CBCT). Skeletal Radiol. 2013;42:649–657. [PubMed: 22990597]
6. Daly MJ, Siewerdsen JH, Moseley DJ, Jaffray DA, Irish JC. Intraoperative cone-beam CT for guidance of head and neck surgery: assessment of dose and image quality using a C-arm prototype: cone-beam CT-guided head and neck surgery. Med Phys. 2006;33:3767–3780. [PubMed: 17089842]
7. Schafer S, Nithiananthan S, Mirota DJ, et al. Mobile C-arm cone-beam CT for guidance of spine surgery: image quality, radiation dose, and integration with interventional guidance: mobile c-arm CBCT in spine surgery. Med Phys. 2011;38:4563–4574. [PubMed: 21928628]
8. Helm PA, Teichman R, Hartmann SL, Simon D. Spinal navigation and imaging: history, trends, and future. IEEE Trans Med Imaging. 2015;34:1738–1746. [PubMed: 25594965]
9. Hirota S, Nakao N, Yamamoto S, et al. Cone-beam CT with flat-panel-detector digital angiography system: early experience in abdominal interventional procedures. Cardiovasc Intervent Radiol. 2006;29:1034–1038. [PubMed: 16988877]
10. Wallace MJ, Kuo MD, Glaiberman C, et al. Three-dimensional C-arm cone-beam CT: applications in the interventional suite. J Vasc Interv Radiol. 2008;19:799–813. [PubMed: 18503893]
11. Orth RC, Wallace MJ, Kuo MD, Technology Assessment Committee of the Society of Interventional Radiology. C-arm cone-beam CT: general principles and technical considerations for use in interventional radiology. J Vasc Interv Radiol. 2008;19:814–820. [PubMed: 18503894]
12. Jaffray DA, Siewerdsen JH, Wong JW, Martinez AA. Flat-panel cone-beam computed tomography for image-guided radiation therapy. Int J Radiat Oncol Biol Phys. 2002;53:1337–1349. [PubMed: 12128137]

13. L etourneau D, Wong JW, Oldham M, et al. Cone-beam-CTguided radiation therapy: technical implementation. Radiother Oncol. 2005;75:279–286. [PubMed: 15890424]
14. Boone JM, Nelson TR, Lindfors KK, Seibert JA. Dedicated breast CT: radiation dose and image quality evaluation. Radiology. 2001;221:657–667. [PubMed: 11719660]
15. Chen B, Ning R. Cone-beam volume CT breast imaging: feasibility study. Med Phys. 2002;29:755–770. [PubMed: 12033572]
16. Zbijewski W, Sisniega A, Stayman JW, et al. High-performance soft-tissue imaging in extremity cone-beam CT In: Medical Imaging 2014: Physics of Medical Imaging (International Society for Optics and Photonics), p. 903329; 2014.
17. Parizel P, Makkat S, Van Miert E, Van Goethem J, Van den Hauwe L, De Schepper A. Intracranial hemorrhage: principles of CT and MRI interpretation. Eur Radiol. 2001;11:1770–1783. [PubMed: 11511901]
18. Kidwell CS, Wintermark M. Imaging of intracranial haemorrhage. Lancet Neurol. 2008;7:256–267. [PubMed: 18275927]
19. Dublin AB, French BN, Rennlck JM. Computed tomography in head trauma. Radiology. 1977;122:365–369. [PubMed: 299951]
20. Smith I, Fleming S, Cernaianu A. Mishaps during transport from the intensive care unit. Crit Care Med. 1990;18:278–281. [PubMed: 2302952]
21. Waydhas C Intrahospital transport of critically ill patients. Crit Care. 1999;3:R83–R89. [PubMed: 11094486]
22. Rumboldt Z, Huda W, All JW. Review of portable CT with assessment of a dedicated head CT scanner. AJNR Am J Neuroradiol. 2009;30:1630–1636. [PubMed: 19661166]
23. Department of Neurosurgery, Hospital Sultanah Aminah, Jalan Persiaran Sultan Abu Bakar, 80100 Johor Bahru, Johor, Malaysia, A.C. Abdullah, Department of Neurosciences, School of Medical Sciences, Universiti Sains Malaysia, Jalan Sultanah Zainab 2, 16150 Kubang Kerian, Kelantan, Malaysia, et al., Limited Evaluation of Image Quality Produced by a Portable Head CT Scanner (CereTom) in a Neurosurgery Centre, MJMS 24, 104–112 (2017) [PubMed: 28381933]
24. Xu J, Sisniega A, Zbijewski W, et al. Modeling and design of a cone-beam CT head scanner using task-based imaging performance optimization. Phys Med Biol. 2016;61:3180–3207. [PubMed: 27025783]
25. Xu J, Sisniega A, Zbijewski W, et al. Technical assessment of a prototype cone-beam CT system for imaging of acute intracranial hemorrhage: technical assessment of CBCT system for ICH imaging. Med Phys. 2016;43:5745–5757. [PubMed: 27782694]
26. Sisniega A, Zbijewski W, Xu J, et al. High-fidelity artifact correction for cone-beam CT imaging of the brain. Phys Med Biol. 2015;60:1415–1439. [PubMed: 25611041]
27. Xu J, Sisniega A, Zbijewski W, et al. Evaluation of detector readout gain mode and bowtie filters for cone-beam CT imaging of the head. Phys Med Biol. 2016;61:5973–5992. [PubMed: 27435162]
28. Wu P, Stayman JW, Mow M, et al. Reconstruction-of-difference (RoD) imaging for cone-beam CT neuro-angiography. Phys Med Biol. 2018;63:115004. [PubMed: 29722296]
29. Sisniega A, Zbijewski W, Wu P, et al. Multi-Motion Compensation for High-Quality Cone-Beam CT of the Head. (The Fifth International Conference on Image Formation in X-Ray Computed Tomography Salt Lake City: UT);2018:4.
30. Wu P, Stayman JW, Sisniega A, et al. Statistical weights for model-based reconstruction in cone-beam CT with electronic noise and dual-gain detector readout. Phys Med Biol. 2018;63:245018. [PubMed: 30524041]
31. Wu P, Sisniega A, Stayman JW, et al. Cone-beam CT statistical reconstruction with a model for fluence modulation and electronic readout noise. In: Medical Imaging 2019: Physics of Medical Imaging (International Society for Optics and Photonics; 2019:1094814.
32. Dang H, Stayman JW, Sisniega A, et al. Multi-resolution statistical image reconstruction for mitigation of truncation effects: application to cone-beam CT of the head. Phys Med Biol. 2017;62:539–559. [PubMed: 28033118]

33. Sisniega A, Zbijewski W, Badal A, et al. Monte Carlo study of the effects of system geometry and antiscatter grids on cone-beam CT scatter distributions. Med Phys. 2013;40:051915. [PubMed: 23635285]
34. Sisniega A, Zbijewski W, Wu P, et al. Image quality, scatter, and dose in compact CBCT systems with flat and curved detectors. In: Medical Imaging 2018: Physics of Medical Imaging. International Society for Optics and Photonics; 2018:105734E.
35. Hsieh J, Gurmen OE, King KF. Recursive correction algorithm for detector decay characteristics in CT. In: Medical Imaging 2000: Physics of Medical Imaging. International Society for Optics and Photonics; 2000:298–305.
36. Poludniowski G, Evans PM, Kavanagh A, Webb S. Removal and effects of scatter-glare in cone-beam CT with an amorphous-silicon flat-panel detector. Phys Med Biol. 2011;56:1837–1851. [PubMed: 21358018]
37. Joseph PM, Spital RD. A method for correcting bone induced artifacts in computed tomography scanners. J Comput Assist Tomogr. 1978;2:100–108. [PubMed: 670461]
38. Day GJ, Dance DR. X-ray transmission formula for antiscatter grids. Phys Med Biol. 1983;28:1429–1433. [PubMed: 6665036]
39. Sisniega A, Stayman JW, Yorkston J, Siewerdsen JH, Zbijewski W. Motion compensation in extremity cone-beam CT using a penalized image sharpness criterion. Phys Med Biol. 2017;62:3712–3734. [PubMed: 28327471]
40. Hansen N, Kern S. Evaluating the CMA evolution strategy on multimodal test functions In: Yao X, Burke EK, Lozano JA, eds. Parallel Problem Solving from Nature - PPSN VIII. Berlin, Heidelberg: Springer; 2004:282–291.
41. Huber PJ. Robust estimation of a location parameter In: Breakthroughs in Statistics, New York, NY: Springer;1992: 492–518.
42. Wu P, Sisniega A, Stayman JW, et al. Clinical study of soft-tissue contrast resolution in cone-beam CT of the head using multi-resolution PWLS with multi-motion correction and an electronic noise model In: 15th International Meeting on Fully Three-Dimensional Image Reconstruction in Radiology and Nuclear Medicine. International Society for Optics and Photonics; 2019:110720B.
43. Erdogan H, Fessler JA. Ordered subsets algorithms for transmission tomography. Phys Med Biol. 1999;44:2835–2851. [PubMed: 10588288]
44. Long Y, Fessler JA, Balter JM. 3D forward and back-projection for x-ray CT using separable footprints. IEEE Trans Med Imaging. 2010;29:1839–1850. [PubMed: 20529732]
45. Wang AS, Stayman JW, Otake Y, et al. Soft-tissue imaging with C-arm cone-beam CT using statistical reconstruction. Phys Med Biol. 2014;59:1005–1026. [PubMed: 24504126]
46. Canny J A computational approach to edge detection. IEEE Trans Pattern Anal Mach Intell. 1986;8:679–698. [PubMed: 21869365]
47. Fessler JA. Mean and variance of implicitly defined biased estimators (such as penalized maximum likelihood): applications to tomography. IEEE Trans Image Process. 1996;5:493–506. [PubMed: 18285134]
48. Star-Lack J, Sun M, Kaestner A, et al. Efficient scatter correction using asymmetric kernels. In: Medical Imaging 2009: Physics of Medical Imaging, International Society for Optics and Photonics; 2009:72581Z.
49. Maier J, Berker Y, Sawall S, Kachelrieß M. Deep scatter estimation (DSE): feasibility of using a deep convolutional neural network for real-time x-ray scatter prediction in cone-beam CT. In: Medical Imaging 2018: Physics of Medical Imaging, International Society for Optics and Photonics; 2018:105731L.
50. Siddon RL. Fast calculation of the exact radiological path for a three-dimensional CT array. Med Phys. 1985;12:252–255. [PubMed: 4000088]
51. Peters TM. Algorithms for fast back- and re-projection in computed tomography. IEEE Trans Nucl Sci. 1981;28:3641–3647.
52. Nesterov Y Smooth minimization of non-smooth functions. Math Program. 2005;103:127–152.
53. Wang AS, Stayman JW, Otake Y, Vogt S, Kleinszig G, Siewerdsen JH. Accelerated statistical reconstruction for C-arm cone-beam CT using Nesterov's method: accelerated CBCT statistical reconstruction using Nesterov's method. Med Phys. 2015;42:2699–2708. [PubMed: 25979068]

54. Sisniega A, Stayman JW, Capostagno S, Weiss CR, Ehtiati T, Siewerdsen JH. Convergence criterion for MBIR based on the local noise-power spectrum: Theory and implementation in a framework for accelerated 3D image reconstruction with a morphological pyramid In: Matej S, Metzler SD, 15th International Meeting on Fully Three-Dimensional Image Reconstruction in Radiology and Nuclear Medicine, SPIE, Philadelphia, USA; 2019:94.

55. Stayman JW, Otake Y, Prince JL, Khanna AJ, Siewerdsen JH. Model-based tomographic reconstruction of objects containing known components. IEEE Trans Med Imaging. 2012;31:1837–1848. [PubMed: 22614574]

56. Uneri A, Zhang X, Yi T, et al. Known-component metal artifact reduction (KC-MAR) for cone-beam CT. Phys Med Biol. 2019;64:165021. [PubMed: 31287092]

57. Dang H, Stayman JW, Xu J, et al. Task-based statistical image reconstruction for high-quality cone-beam CT. Phys Med Biol. 2017;62:8693–8719. [PubMed: 28976368]

58. Tilley S II, Sisniega A, Siewerdsen JH, Stayman JW. High-fidelity modeling of detector lag and gantry motion in CT Reconstruction; arXiv:1805.11631:[physics]; 2018.

59. Sisniega A, Capostagno S, Zbijewski W, Weiss CR, Ehtiati T, Siewerdsen JH. Image-based deformable motion compensation for interventional cone-beam CT In Bosmans H, Chen G-H, Gilat ST, eds. Medical Imaging 2019: Physics of Medical Imaging. San Diego, USA: SPIE; 2019:59.

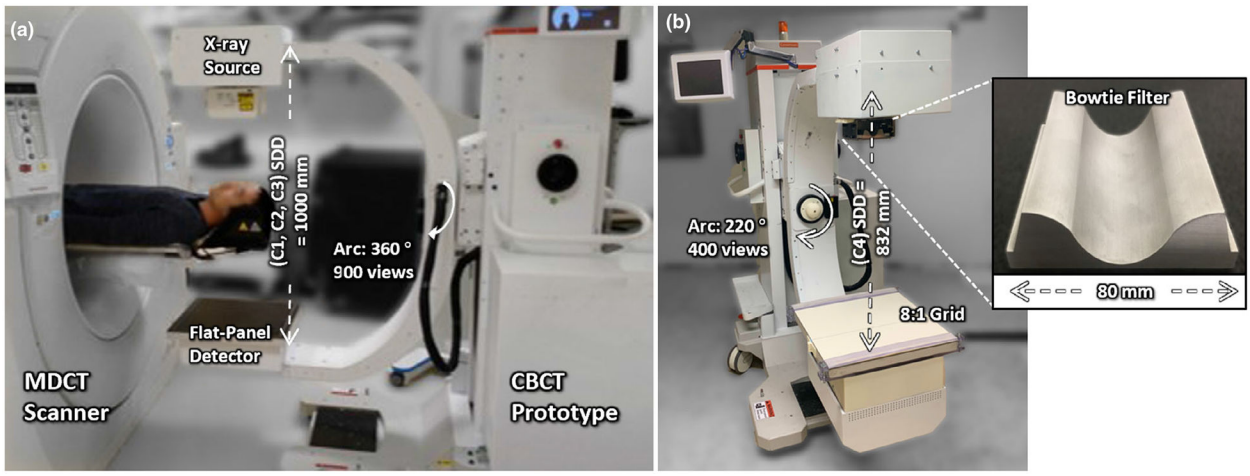

Fig. 1.

Prototype scanner for high-quality cone-beam computed tomography (CBCT) of the head. (a) Arrangement of the CBCT prototype (C1 configuration) for scanning human subjects. (b) Head scanner prototype (C4 configuration) featuring a more compact system geometry, an 8:1 antiscatter grid on the detector, and a bowtie filter.

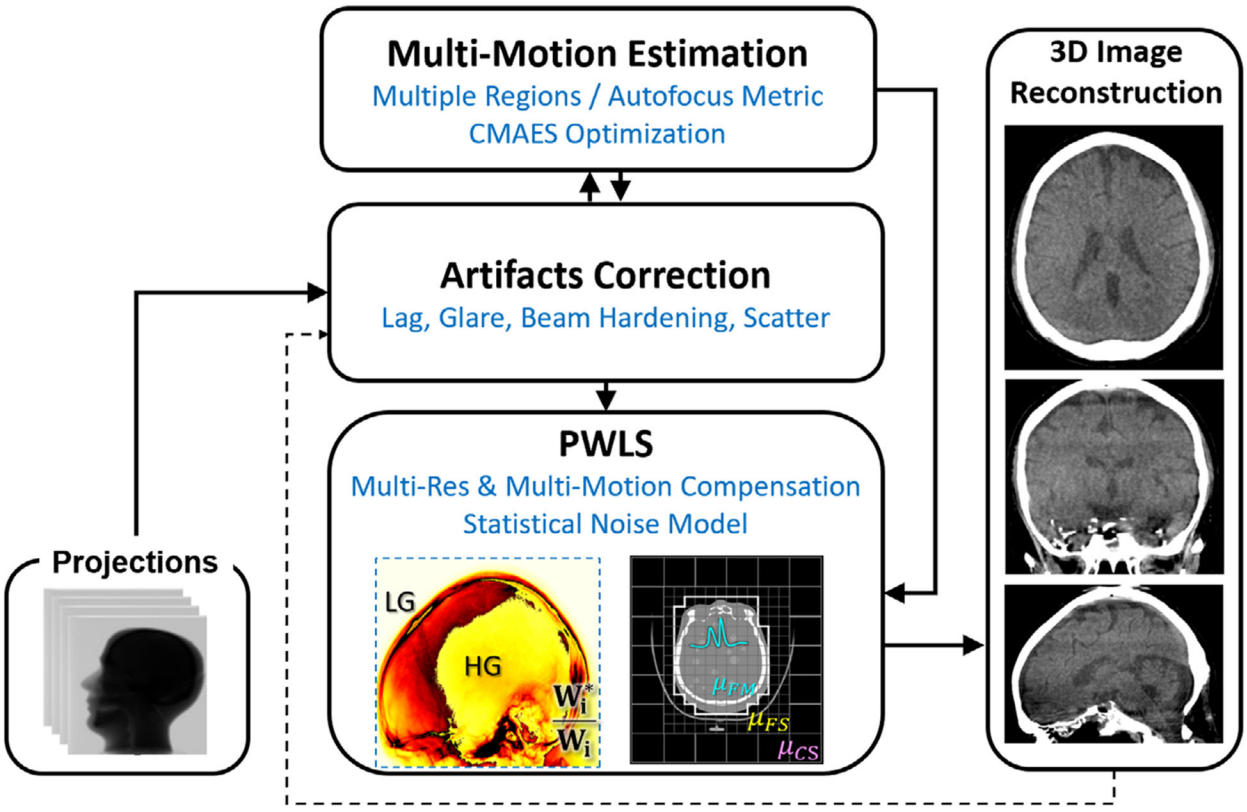

Fig. 2.

Flowchart for the artifacts correction and image reconstruction workflow. Note the interconnection of artifact corrections with multi-motion estimation (double arrows) and feedback loop of the penalized weighted least squares image (dashed arrow) to artifact correction (x-ray scatter) in the final iteration.

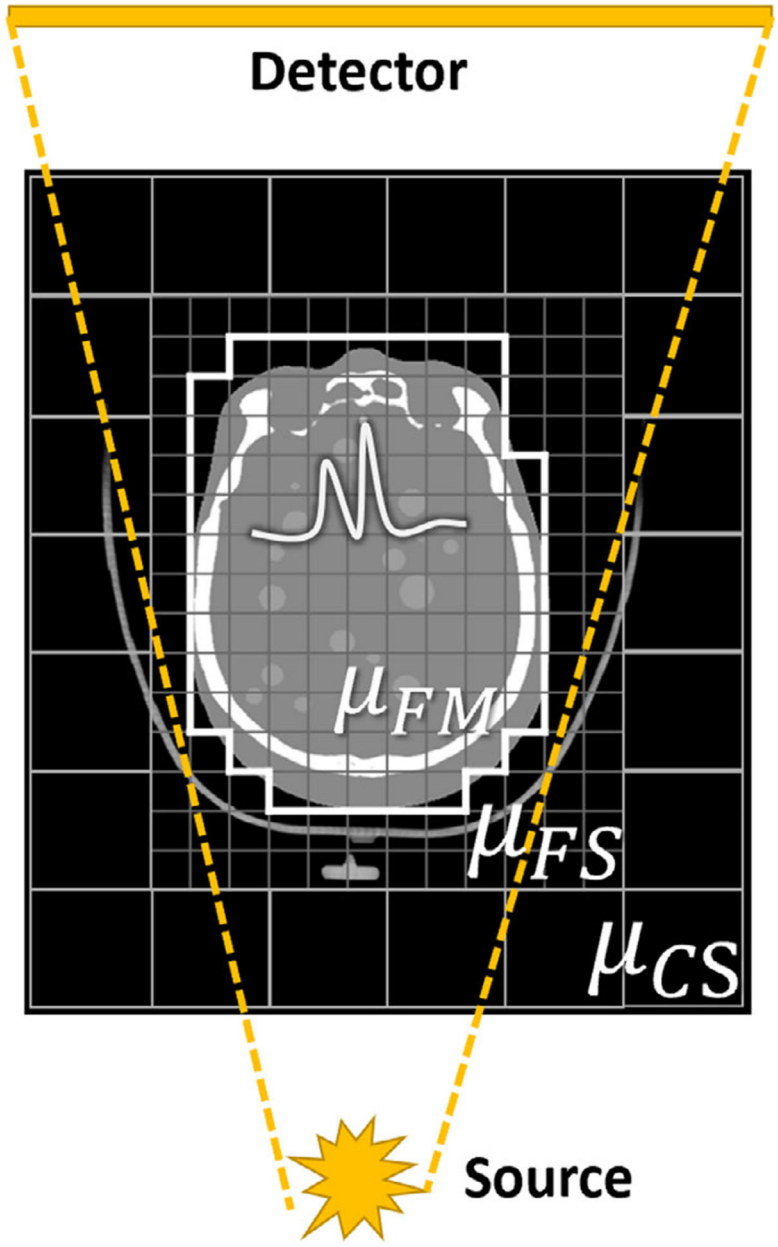

Fig. 3.

Illustration of three regions in dual-motion, dual-resolution image reconstruction: μ_{FM}, μ_{FS}, and μ_{CS}, where the "M" and "S" notation denotes the "moving" and "static" regions for the multi-motion estimation, and the "F" and "C" notation denotes the "fine" and "coarse" regions for multiresolution reconstruction.

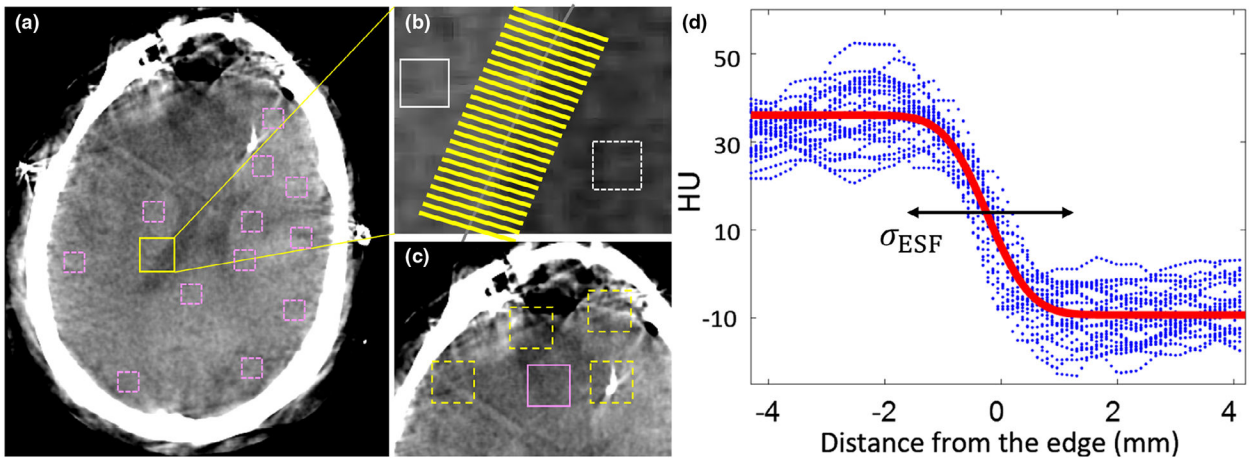

Fig. 4.

Analysis of noise, spatial resolution, and artifacts in human subject images. (a) Example reconstruction showing ROI placement for analysis of NU (pink ROIs) and spatial resolution (yellow ROI). (b) Zoomed-in region showing the soft-tissue boundary (between the lateral ventricle and brain parenchyma) and edge profiles (yellow lines) for measurement of the ESF at soft-tissue boundaries. ROIs for contrast measurement are marked by white rectangles. (c) Zoomed-in image showing ROI placement for calculation of streak artifacts, σ_{streaks}, in motion-contaminated regions (dashed yellow ROIs) and uniform regions (solid pink ROI). (d) Example ESF analysis from profiles perpendicular to the soft-tissue boundary in (b). The width (σ_{ESF}) of the fitted error function (solid red line) provided a basic metric of spatial resolution with respect to the soft-tissue edge.

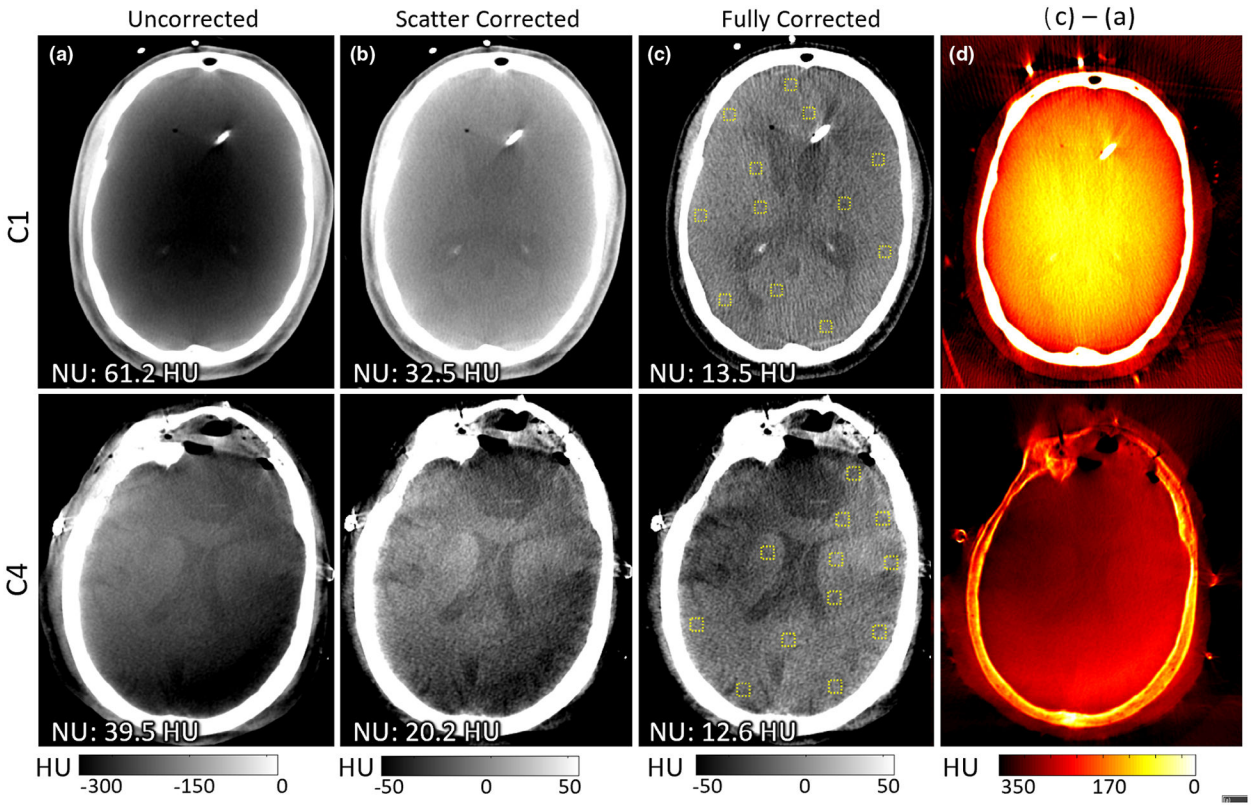

Fig. 5.

Artifact corrections. Images reconstructed with filtered backprojection (FBP) are shown at different stages of the artifacts correction pipeline: (Top) C1 configuration; (Bottom) C4 configuration, incorporating a bowtie filter and an antiscatter grid. (a) Uncorrected image. (b) Scatter-corrected image. (c) Fully corrected image. Dashed squares show ROIs for NU measurement. (d) Difference image (c–a) showing the magnitude and distribution of artifacts. Corresponding NU measurement are listed in the bottom left corner for each subfigure in column (a–c).

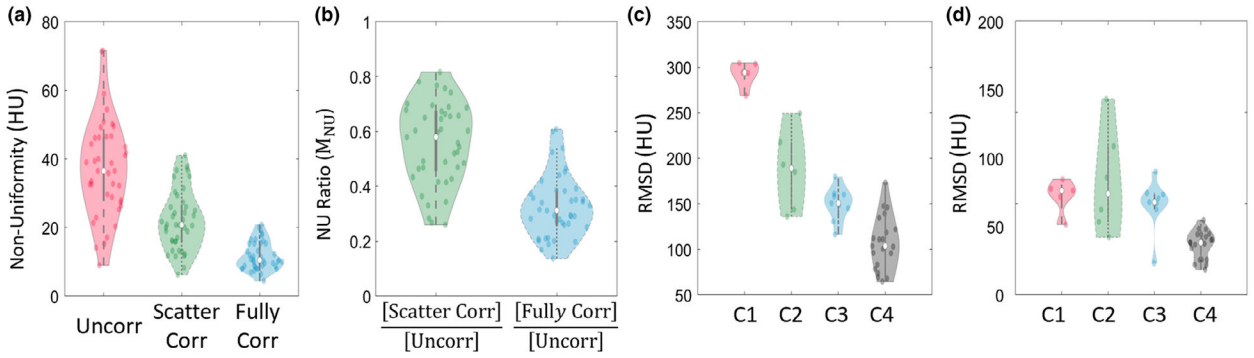

Fig. 6.

Quantitative analysis of the artifacts correction pipeline aggregated over 41 subjects in the study. Each violin plot shows the underlying sample points, a Gaussian envelope, the median of the distribution (white circle), and the interquartile range (IQR, black vertical range bar). (a) Nonuniformity measured at three stages of the artifacts correction pipeline. (b) Relative improvement in NU, comparing images corrected for scatter only and fully corrected images (corrected for lag, glare, beam-hardening, and scatter). (c) Difference (RMSD) between uncorrected and fully corrected data for the four configurations of the scanner prototype (C1–C4), showing increasing improvement in the quality of raw data for later configurations. (d) Difference (RMSD) between scatter-corrected and fully corrected images as a function of the system configuration.

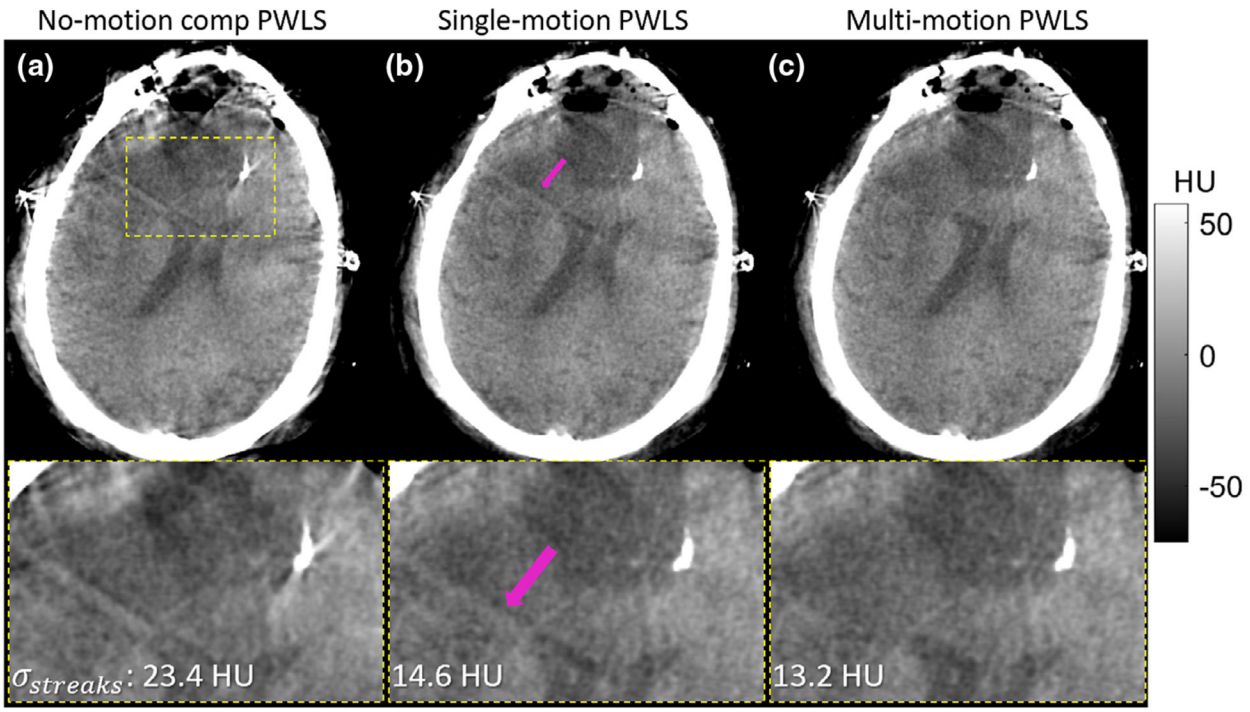

Fig. 7.

Motion compensation. (a) Example image reconstructed without motion compensation. (b) PWLS reconstruction with single-motion compensation (i.e., motion trajectory computed for the head applied to the entire volume). (c) Multi-motion compensation PWLS reconstruction allowing separate motion trajectories for the head and the holder. The lower row shows a zoomed-in region (dashed yellow rectangle in (a)) containing a hypodensity (edema) and a ventricular shunt along with corresponding quantitation of the streak artifacts (σ_{streaks}).

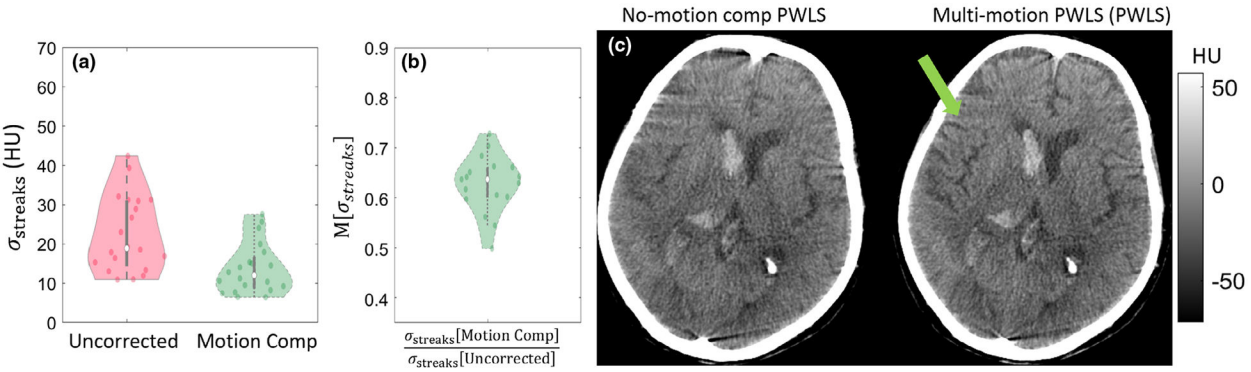

Fig. 8.

Quantitative analysis and illustration of motion compensation. (a) Magnitude of streak artifacts (σ_{streaks}) for uncorrected and motion compensated images. (b) The ratio of improvement in the magnitude of streak artifacts (M[σ_{streaks}]) evaluated for 25 subjects exhibiting visible streak artifacts prior to motion compensation. (c) A representative dataset from a subject with intraventricular hemorrhage showing improved soft-tissue visibility from motion compensation — for example, improved visualization of sulci in the region marked by the green arrow.

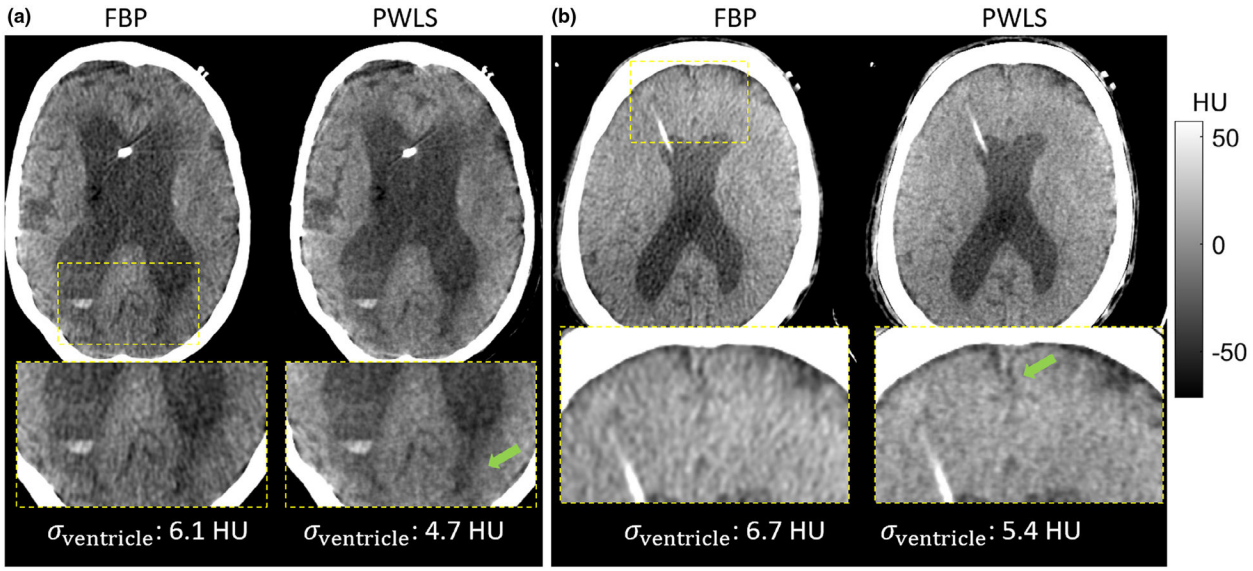

Fig. 9.

Comparison of filtered backprojection (FBP) and penalized weighted least squares (PWLS) reconstruction for two example subjects, each with zoomed-in regions showing features of interest in the bottom row. Subtle improvement in low-contrast structures can be appreciated for PWLS. For example, visually improved delineation of the sagittal sulcus and lateral aspect of the ventricle can be observed, as marked by green arrows.

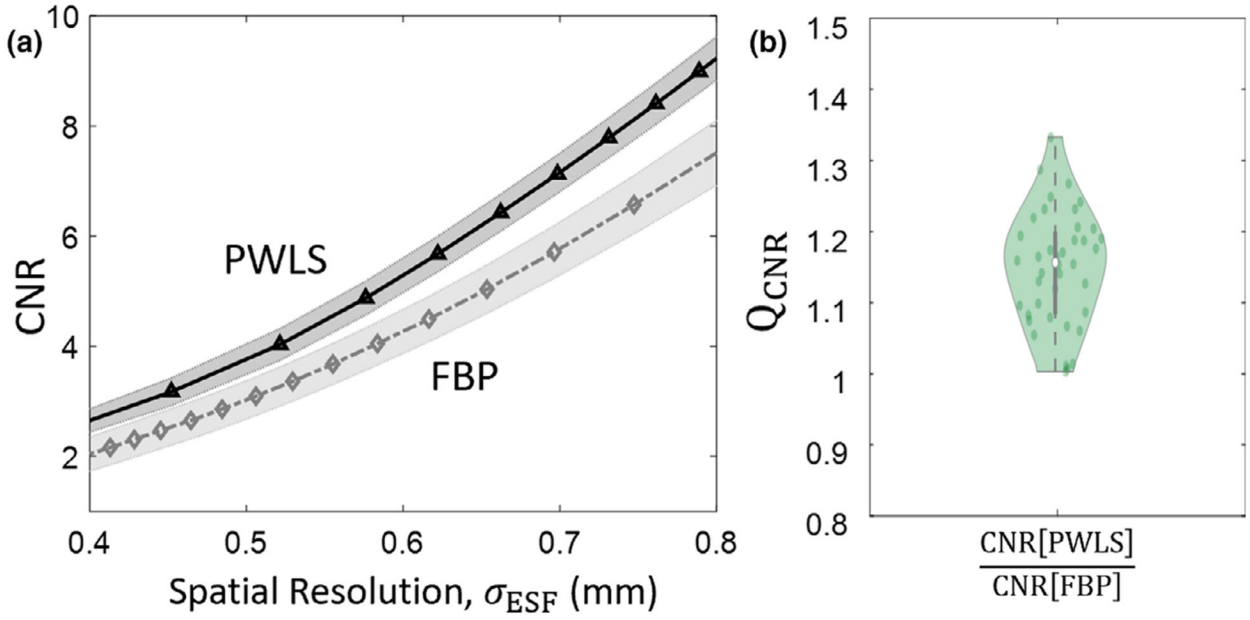

Fig. 10.

Analysis of soft-tissue contrast-to-noise ratio (CNR) (ventricle-to-parenchyma) for filtered backprojection (FBP) and penalized weighted least squares (PWLS) reconstructions measured over the 41 subjects. (a) contrast-to-noise ratio evaluated as a function of edge-spread width (σ_{ESF}) for an example subject [same as in Fig. 9(a)] obtained by changing the cutoff frequency and β parameters for FBP and PWLS, respectively. The gray range about each curve denotes the standard deviation in CNR estimated from fits to various edge profiles, as shown in Fig. 4(b). (b) Relative improvement in CNR. The violin plot shows sample points, Gaussian fit envelope, median (1.15), and IQR (1.02–1.32).

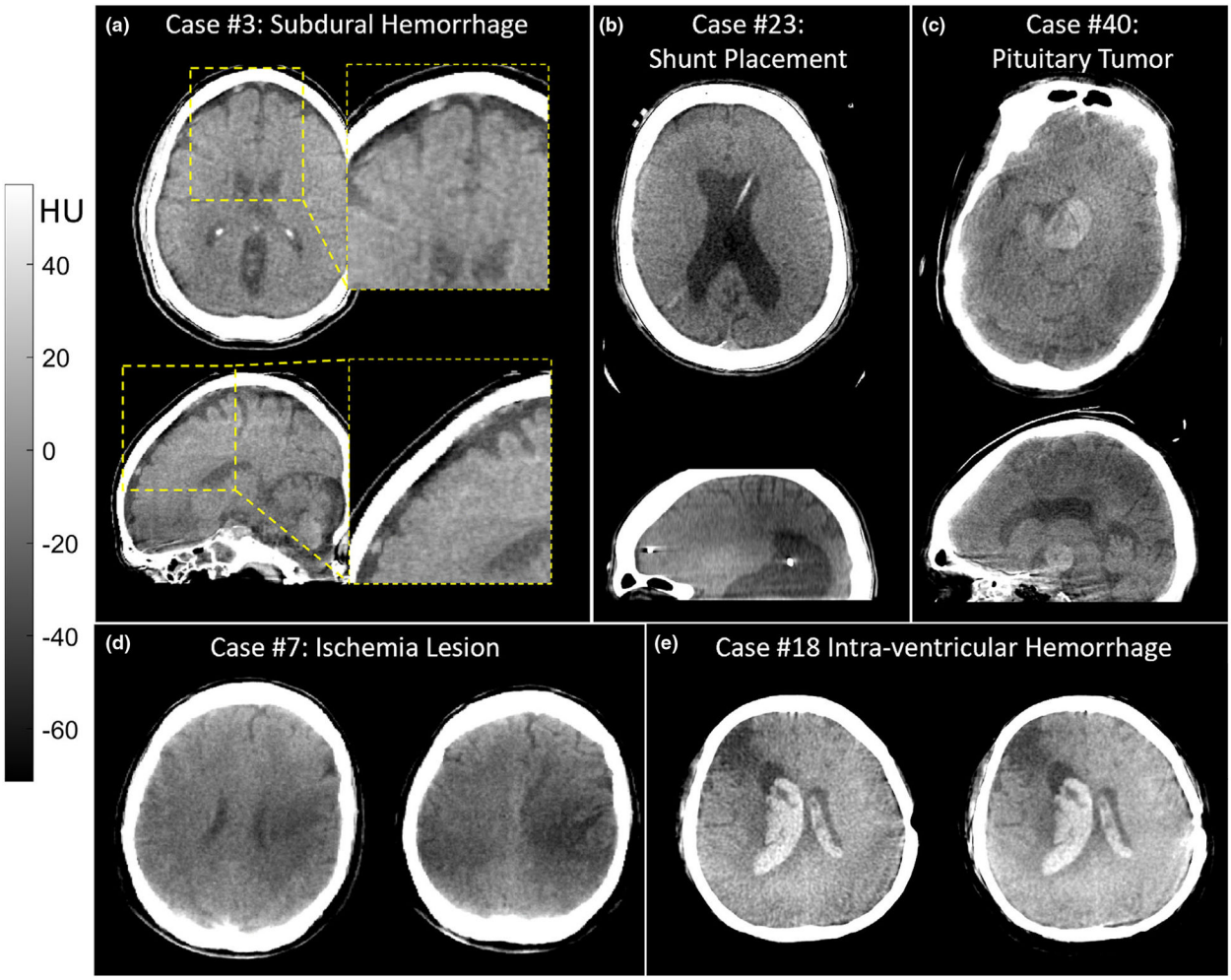

Fig. 11.

Example cone-beam computed tomography images illustrating a variety of clinically relevant tasks. (a) Subject with subdural hematoma evident as a hyperdense focus between the brain parenchyma and skull. (b) Subject with hydrocephalus treated with a ventricular shunt. (c) Subject with hemorrhagic pituitary tumor, evident as a hyperdense mass adjacent to the skull base. (d) Subject with bilateral ischemic lesions evident as hypodensities. (e) Subject with intraventricular hemorrhage (hyperdensity in both lateral ventricles).

Table I.

Hardware configurations and image acquisition parameters used in the human subjects study. The C4 configuration represents the primary configuration for the majority of subjects (stratification detailed in Section 2.C).

Config	SAD (mm)	SDD (mm)	kV	# Proj	Arc (°)	Tscan (s)	Dw (mGy)	Grid	Bowtie	FOVz (cm)	Mode	# Subjects
C1	550	1000	100	450	360	30	24	No	No	24	4 × 2 DG	5
C2	550	1000	100	900	360	60	38	No	No	12	4 × 2 DG	6
C3	550	1000	100	900	360	60	38	8:1	No	12	4 × 2 DG	9
C4	550	832	120	400	220	17	29	8:1	Custom	24	3 × 3HG	21